ADVANCED FUNCTIONAL MATERIALS

Supporting Information

for *Adv. Funct. Mater.*, DOI: 10.1002/adfm.202008380

Stimuli Responsive Shape Memory Microarchitectures

*Luizetta V. Elliott, Erika E. Salzman, and Julia R. Greer**

Supporting Information

Stimuli Responsive Shape Memory Micro-Architectures

*Luizetta V. Elliott, Erika E. Salzman, Julia R. Greer**

Number of elastically active chains

The number of elastically active chains per unit volume was estimated using Kuhn's affine network model.[1] The number of elastically active chains per unit volume is given by **Equation S1**:

$$\frac{n}{V} = \frac{G}{k_B T} \quad \text{(S1)}$$

Where n is the number of chains, V is the volume, G is the shear modulus, k_B is Boltzmann's constant and T is the temperature in Kelvin. The value of G was estimated based on the elastic modulus typical for a benzyl methacrylate based shape memory network (~10MPa),[2] and the relationship in **Equation S2**.

$$E = 2G(1 + v) \quad \text{(S2)}$$

Here E is the elastic modulus, G is the shear modulus and v is the Poisson's ration, taken here to be 0.5, as is typical for a rubber. The temperature was taken to be 100^0 C, which is reliably in the rubbery plateau for these networks.

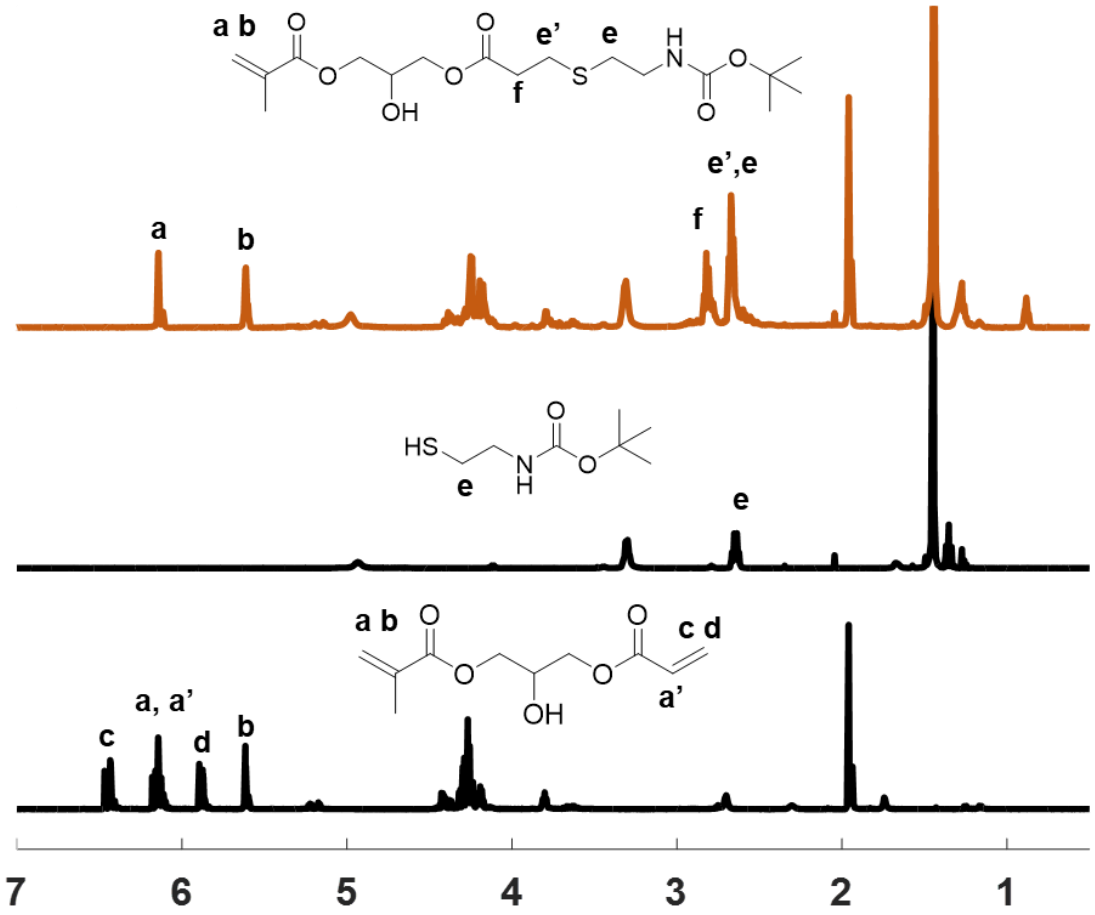

Figure S1. Chain builder functionalization. a) ^{1}H NMR of the thiol-Michael addition product used as the functional chain builder. Peaks corresponding to methacrylate hydrogens are highlighted, as well as those corresponding to the reacted acrylate groups. b) ^{1}H NMR spectrum of the 2-(BOC-amino) ethanithiol starting material. c) ^{1}H NMR spectrum of the 3-(acryloyloxy)-2-hydroxypropylmethacrylate starting material. Peaks corresponding to the acrylate and methacrylate groups are noted.

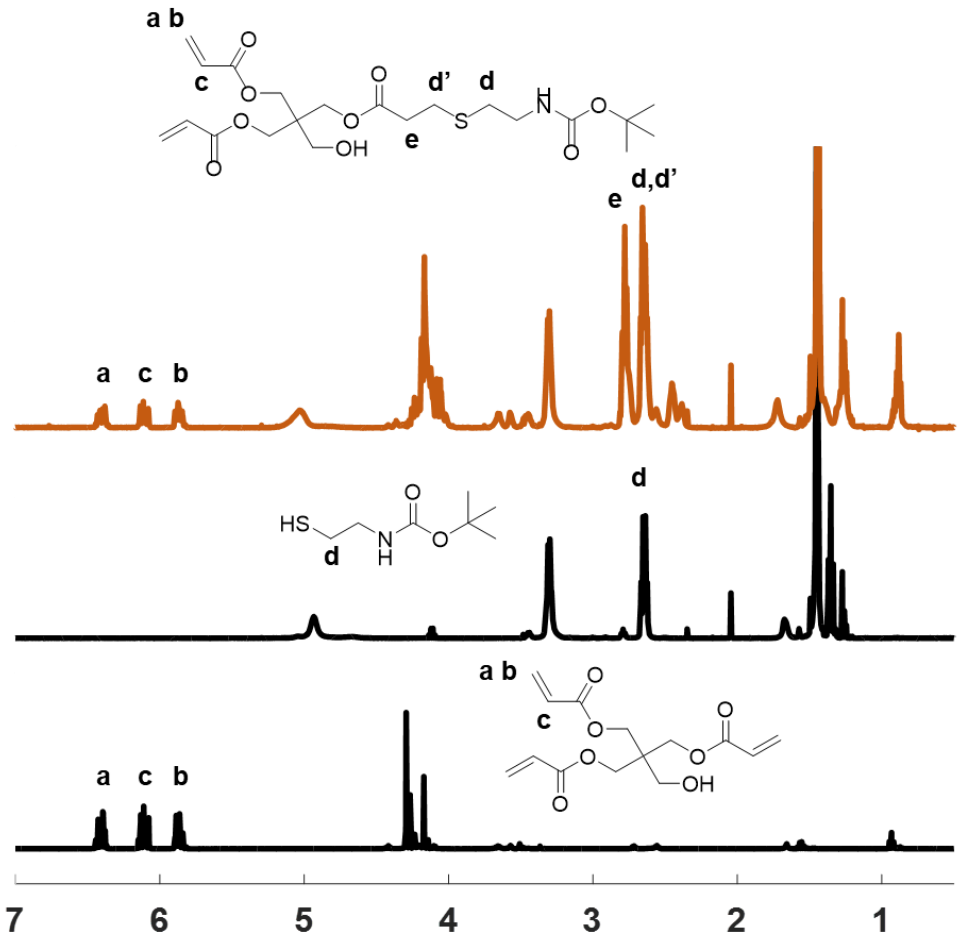

Figure S2. Crosslinker functionalization. a) ^{1}H NMR spectrum of the thiol-Michael product used as the crosslinker. Beaks corresponding to reacted and unreacted acrylate groups are highlighted. b) ^{1}H NMR spectrum of the BOC-ethanethiol starting material. c) ^{1}H NMR spectrum of the of pentaerythritol triacrylate starting material. Peaks corresponding to the acrylate groups are highlighted.

Wave number [cm^{-1}]	Feature
940-960	Silicon chip
1004, 1030	Benzene ring breathing, deformation (in plane)
1130-1215	Benzene ring deformation (in plane)
1370-1380	CH_3 symmetric bending
1450	CH_2 scissoring
1585-1605	Aromatic C=C stretching
1635	Aliphatic C=C stretching
1730	C=O stretching

Table S1. Raman spectroscopy peak identification.[3,4]

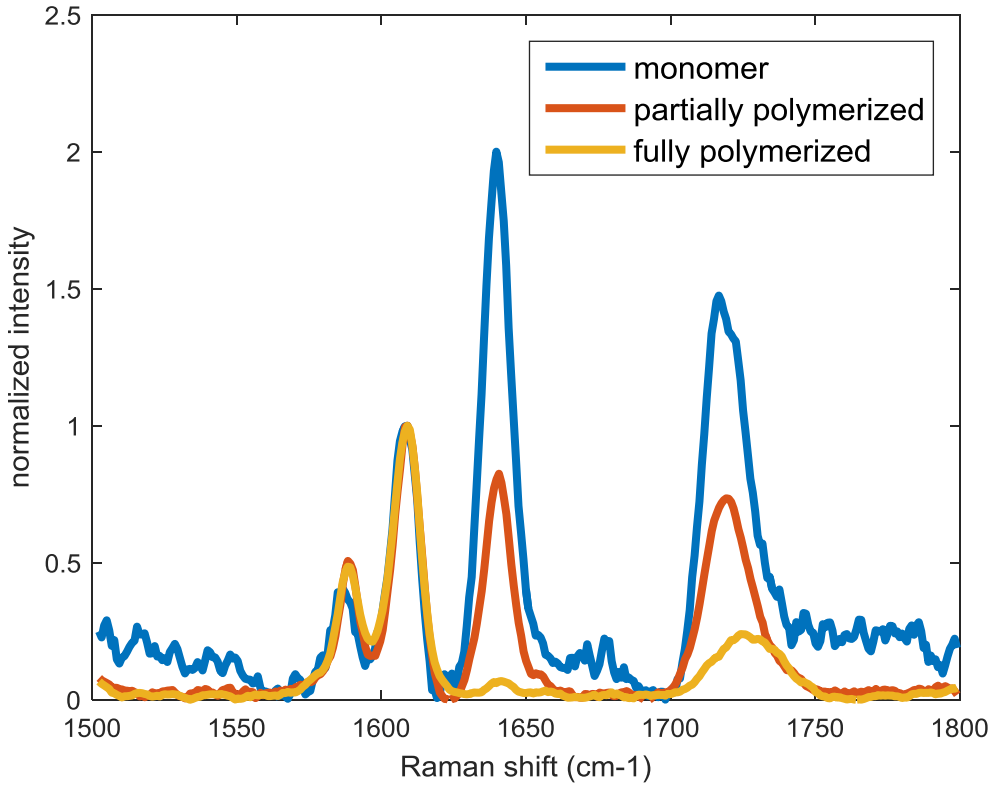

Figure S3. Representative Raman spectra used to determine benzyl methacrylate degrees of polymerization. Intensities are normalized by the aromatic C=C stretch peak at 1605 cm^{-1}.

Degree of Polymerization

Raman spectroscopy was performed on pre-polymerized BMA to ensure that acrylate groups were available for further reaction during two photon polymerization. To estimate the degree of polymerization, the peak areas corresponding to aromatic (1605 cm^{-1}) and aliphatic (1635 cm^{-1}) carbon double bonds were determined by trapezoidal numerical integration.[4] The ratio of these areas for the polymerized material and the starting monomer were then compared as previously established, since, unlike the carbonyl C=O stretch (1730 cm^{-1}), the aromatic C=C stretch peak is not expected to be affected by polymerization. The degree of polymerization was defined by **Equation S3**:

$$DP\% = \left(1 - \frac{R_{polymer}}{R_{monomer}}\right) * 100\% \qquad R = \frac{A_{aliphatic}}{A_{aromatic}} \qquad \text{(S3)}$$

The calculation was performed based on 3 samples of pre-polymerized BMA. A set of representative Raman spectra, normalized by the aromatic peak at 1605 cm^{-1}, is provided in **Figure S3**. The degree of polymerization was determined to be 60 $^{+}/_{-}$ 3%. For comparison, the degree of polymerization for BMA exposed to UV light for 1 hour (fully polymerized) was determined to be 97 $^{+}/_{-}$ 1%

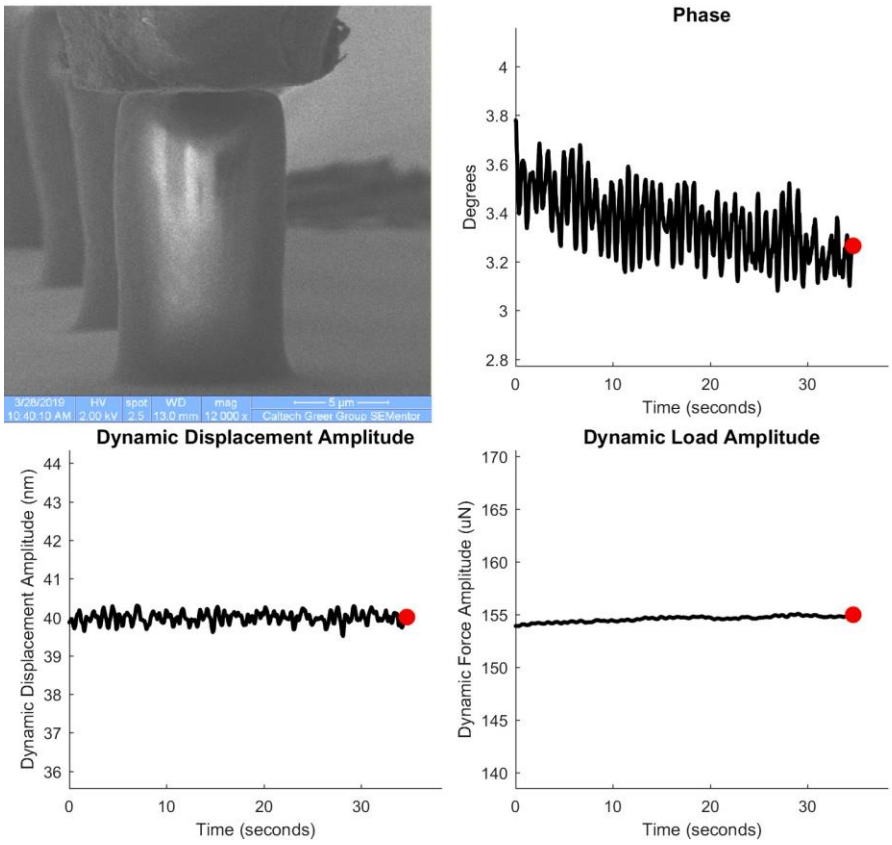

Figure S4. Representative still frame from an *In-situ* DMA experimental video with synchronized raw phase shift, dynamic displacement amplitude and dynamic load amplitude obtained at room temperature.

	Shape fixity	Shape recovery	Recovery time
Cubic lattice	97 +/- 4%	86+/- 4%	174 sec (video S1)
Pillar	80 +/- 30 %	96 +/- 3 %	127 sec (video S2)
Flower	87 +/- 17%	79 +/- 6%	176 sec (video S3)

Table S2: Shape memory characteristics of programmed structures. Recovery times obtained from supporting videos S1-3. N=3.

Shape memory characterization

$R_r = (h_{temporary} - h_{recovered})/(h_{temporary} - h_{original})$ (S4)

$R_f = h_{temporary}/h_{programming}$ (S5)

Shape memory properties of samples with three geometries: lattice, pillar, and flower were characterized through the shape recovery ratio (**Equation S4**), the shape fixity ratio (**Equation S5)** and the shape recovery time (**Table S2**). The in-situ programming conditions are most conducive to quantifying shape recovery in cubic lattices and pillars. The following limitations apply to other parameters and structures:

1) Determining the shape fixity values requires quantifying total deformation i.e. the deformation during the programming step while the sample is in contact with the indenter. To approximate this value, we utilized the distance between the edge of the indenter tip and the base of the sample. Obstruction of the full sample view by the indenter tip is a possible source of error that could be causing the substantial standard deviation.
2) The measured recovery times are influenced by the experimental setup because the sample is not immediately heated to the target recovery temperature. Heating during recovery occurs at the maximum rate allowed by the instrument (10°C/min), and the reported recovery time reflects the combined material response over this evolving temperature profile.

3) We isolated vertical deformation to determine the shape fixity and recovery ratios for cubic lattices and pillars; the appropriate deformation metric for more complex structures, such as a flower, is less clear. We chose to track the bending angle of a set of petals as the representative parameter

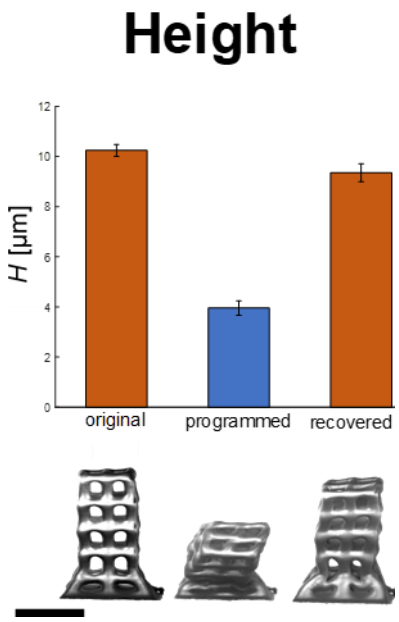

Figure S5. Lattice height in µm before programming, in the programmed state and after recovery, with representative sample images displayed below. Scale bar 5µm. Error bars represent one standard deviation, n=3

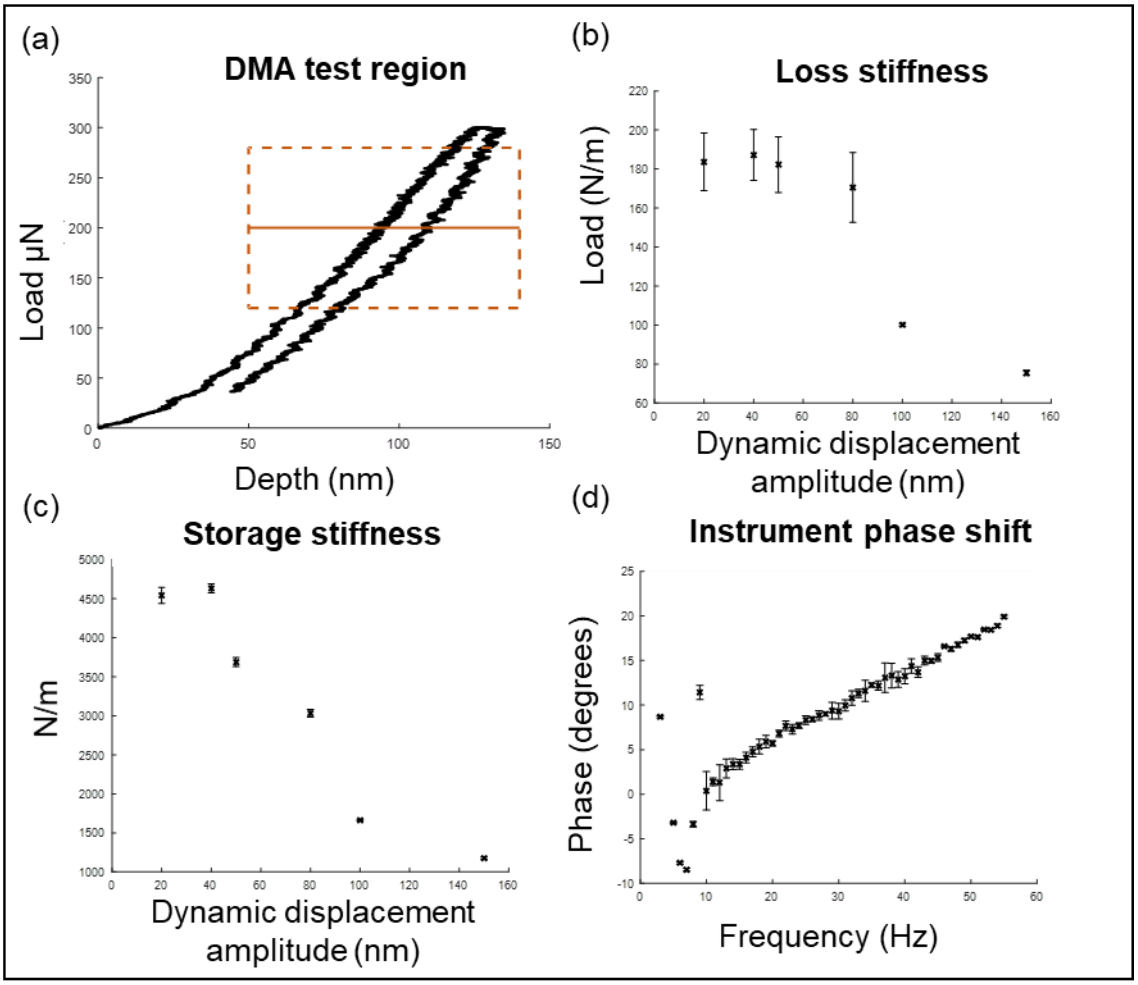

Figure S6. DMA conditions validation. a) Sample loading/unloading curve for the synthesized pillars at room temperature. The solid line indicates the pre-load used in the DMA experiment, while the dashed box outlines the maximum load amplitude detected during the test. c) Sample loss stiffness determined at various target dynamic displacement amplitudes. Black box correction applied at each target displacement. n=3. d) Sample storage stiffness determined at various target dynamic displacement amplitudes. Black box correction applied at each target displacement. n=3. d) Instrument phase shift as a function of temperature obtained by oscillating in vacuum. n=3.

Viscoelastic Region

To verify that the DMA experiments were conducted within the viscoelastic region of the material, pillars were loaded to 300μN at a rate of 10 μN/s, held for 10s and unloaded (**Figure S6a**). After contact was established, linear loading was observed, followed by unloading with some hysteresis, as is characteristic of a viscoelastic material. During DMA experiments at 40nm target displacement amplitude, the maximum load amplitude observed was 160μN. Therefore, it was expected that the sample would remain within the viscoelastic range and that contact would be maintained. A variety of dynamic displacement amplitudes were then tested on a series of pillars in 10Hz DMA experiments (**Figure S6b-c**).[5] For amplitudes of 50nm and greater, an increase in loss modulus, decreases in storage and loss stiffness, as well as an increase in the tangent delta were observed. For the lower values of 20nm and 40nm, however, these values remained constant, indicating viscoelasticity. The material was therefore determined to be within its viscoelastic region for a pre-compression of 200 μN and a 40nm amplitude 10 Hz DMA experiment.

Figure S7. Instrument tangent delta as well as storage and loss moduli in vacuum obtained by tip equilibration at each target temperature. Orange line indicates the line of best fit obtained from linear regression.

Black box correction

DMA experiments were performed on a nanomechanical instrument that applies force to an indenter column which is supported by springs that restrict motion in one direction. This results in interaction with the sample through a flat punch tip, and a corresponding displacement measured through a capacitive gage. When an oscillatory force is applied, a lock in amplifier is used to isolate the load and displacement signals that occur at the target frequency, allowing the corresponding amplitudes as well as the phase shift to be measured. However, these measured values represent the combined response of the sample and the

indenter system. This interaction can be represented by a mechanical model (**Figure 3b**), allowing the dynamic response of the sample to be isolated from some features of the instrument.[5] In particular, the is expected that both the sample and the support springs will contribute to the measured storage stiffness, while the loss stiffness will be affected by the damping between capacitive plates. They are therefore represented as springs and dashpots, respectively.

The obtained data were corrected to account for these contributions. According to the mechanical model, when the indenter is oscillated in vacuum without contacting the sample the storage stiffness observed corresponds only the to the support springs, while the loss stiffness observed corresponds exclusively to dampening between capacitive plates. The stiffness values representing the sample and its contact with the indenter were therefore calculated as follows:

$$k_{storage} = \left|\frac{F_0}{u_0}\right| \cos(\delta) - \left|\frac{F_0}{u_0}\right|_{vacuum} \cos(\delta_{vacuum}) \quad \text{(S6)}$$

$$k_{loss} = \left|\frac{F_0}{u_0}\right| \sin(\delta) - \left|\frac{F_0}{u_0}\right|_{vacuum} \sin(\delta_{vacuum}) \quad \text{(S7)}$$

The calculated stiffnesses correspond to the sample and its contact with the indenter, which are represented by a black box in the mechanical model. This indicates that the values obtained do not rely of any assumptions about the mechanical behavior of the sample material. This also means that the response of the sample cannot be decoupled from the contact between the indenter and the material. However, as the polymer sample is significantly less stiff than the diamond indenter, a deviation of under 3% from the true value is expected.[6,7]

To apply this correction, it was first necessary to validate that the indentation system can be described as a one dimensional oscillator under the target experimental conditions.[4] To do so, the phase angle was measured as a function of frequency in 1Hz increment with the

indenter column oscillating in vacuum at the displacement corresponding to the 200μN sample pre-loading (**Figure S6d**). Between 10Hz and 55 Hz, no discontinuities were observed, which indicates that at this frequency range the difference between stiffnesses in the vertical and lateral directions is sufficiently large to prevent cross-talk. Further, the phase angle did not increase past 90 degree, indicating that the resonant frequency of the instrument was not detected. It was therefore determined that the instrument can be represented by a one dimensional oscillator model in the 10-55Hz frequency range, and the black box mechanical model can be applied.

To apply the black box correction, the indenter tip was oscillated in vacuum at the displacement corresponding to the 200 μN sample pre-loading. The oscillation was initially performed after the tip was equilibrated at each target temperature. However, no temperature dependence in the instrument was observed (**Figure S7**). Therefore, the correction data obtained at room temperature were utilized for all experiments.

To analyze both for correction and sample oscillation data, the DMA portion of the experiment was first isolated. That was done by selecting the region where the observed dynamic displacement was within 10% of the target value for at least 1000 consecutive points. The loss stiffness and storage stiffness were then calculated according to **Equation S6** and **Equation S7**. The ratio between them was then used to determine the corrected tangent delta. At room temperature, applying the correction resulted in a 1% decrease in loss stiffness, 3.9% decrease in storage stiffness, and 2.9% increase in the tangent delta. At 87^0 C, the correction resulted in an 8.8% decrease in storage stiffness, a 0.33% decrease in loss stiffness and an 8.4% increase in the tangent delta.

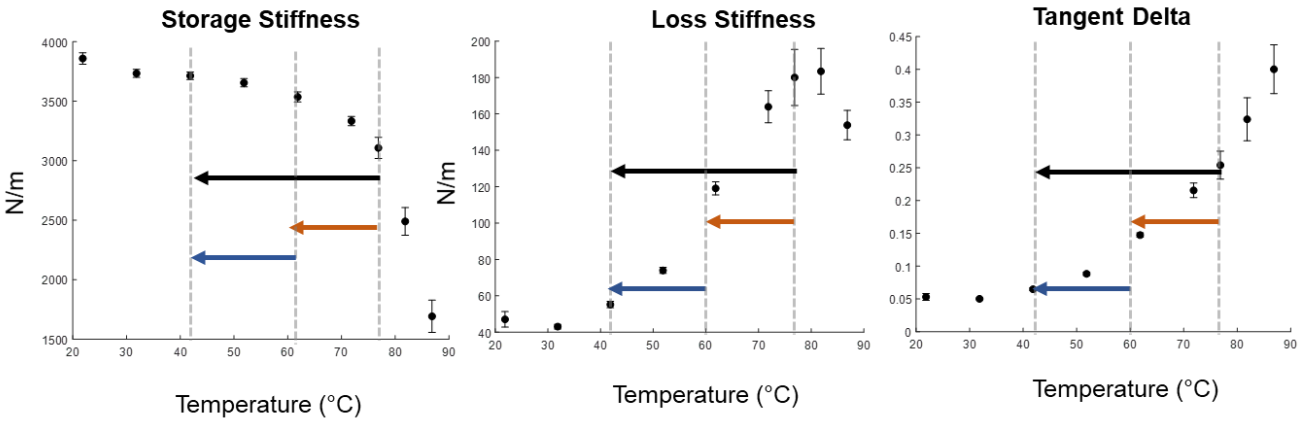

Figure S8. Temperature changes during the programming step of the shape memory cycle overlaid with pillar DnMA data. The original temperature change from 77°C to 42°C under load is illustrated with the black arrow. The orange arrow illustrates high final programming temperature - removing the programing load at 60°C rather than 42°C. The blue arrow illustrates low initial programming temperature - beginning programming by applying load at 60°C rather than 77°C.

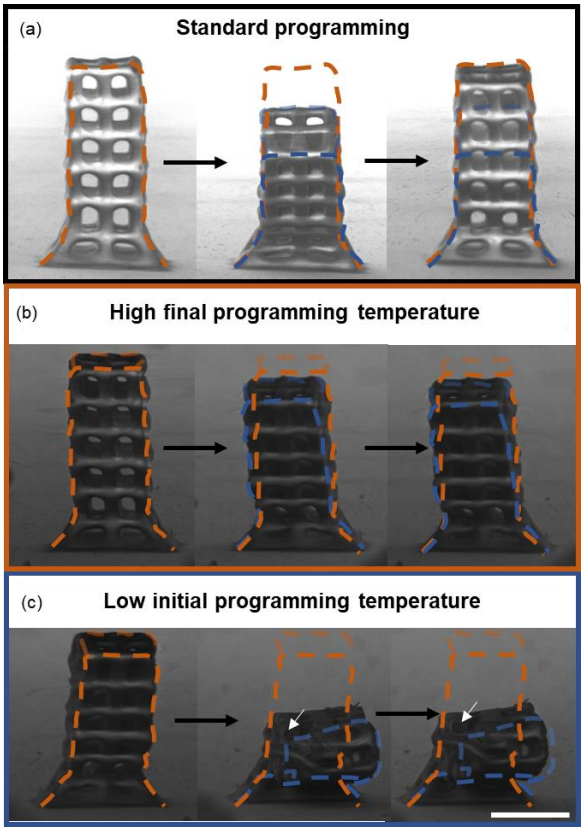

Figure S9. Shape memory effect of 3D lattices programmed (a) using the standard protocol, with load applied at 77°C and removed at 42°C, (b) at a higher final temperature of 60°C, with load applied at 77°C and removed at 60°C, and (c) at a lower initial programming temperature of 60°C, with load applied at 60°C and removed at 42°C. Dashed orange outline corresponds to the original geometry, dashed blue outline represents the programmed structure. White arrows indicate a broken beam. Scale bar 5µm.

Programming temperature effects

The choice of standard programming temperature range of the shape memory cycle is informed by the position of the loss modulus peak at 77°C and by the high storage stiffness, low loss stiffness and low tangent delta at 42°C, which are consistent with a glassy state of the polymer (**Figure S8**). We considered two alternate programming conditions: (1) an increase in the final programming temperature from 42°C to 60°C, where the polymer should not reach a glassy state and (2) a decrease in the initial programming temperature from 77°C to 66°C, where the polymer is insufficiently heated below the loss modulus peak temperature. The thermomechanical properties corresponding to these programming parameters are displayed in **Figure S8**, with the corresponding images of lattices throughout salient points of each programming cycle displayed in **Figure S9**. These results reveal that at high final programming temperature (**Figure S9b**), the structure recovers immediately after the programming step, prior to the application of heat to trigger recovery. Some plastic deformation is observed, likely attributable to lateral drift during programming, and results in a shape recovery ratio of only 8%. In the case of a low initial programming temperature (**Figure S9c**), the load applied during programming results in predominantly plastic deformation, as indicated by the broken beam highlighted in the figure, and marginal shape recovery observed upon heating (shape recovery ratio of 7%). These results support the chosen standard programming temperature range of 42°C to 77°C; effective programming requires polymer chain mobility that emerges at the loss stiffness peak at incipient load application and a sufficient reduction in polymer chain mobility at the final programming temperature to prevent recovery following load removal.

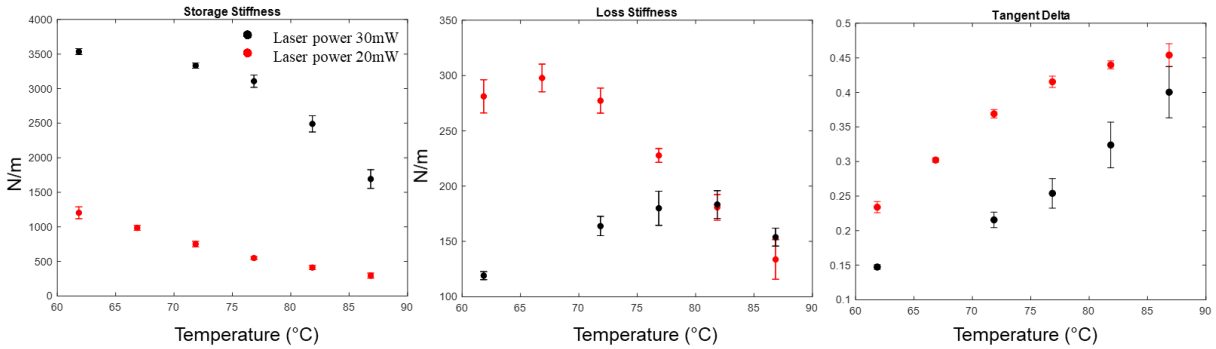

Figure S10 Storage and loss stiffness as well as the tangent delta of the pillars written at 30mWlaser power (black) and 20mW laser power (red).

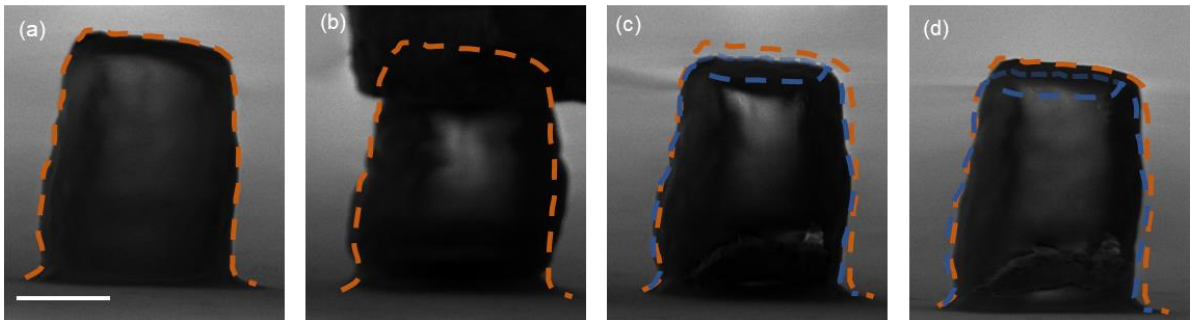

Figure S11. Representative shape memory programming sequence for samples fabricated at a reduced laser power of 20mW that shows (a) a representative as-printed pillar, (b) initial contact with the indenter tip during programming at 67°C, (c) programmed pillar at 42°C, and (d) after recovery at 87 ^{0} C. Orange dashed line outlines the original geometry, blue outline represents programmed state. Scale bar 5µm.

Effects of crosslinking density

Structures fabricated via TPL-DLW are typically characterized by low conversion, with the degree of crosslinking controlled by laser power and scan speed.[8,9] We lowered the laser power from 30mW to 20mW while maintaining a constant scanning speed to decrease the degree of crosslinking and characterized the effect of this change by studying the shape memory response of micro-pillars with a diameter of 8µm.

DnMA was performed to determine the effect of crosslinking density on the glass transition (**Figure S10**). We observed a broadening in the tangent delta curve and a 10°C shift in the loss modulus peak to lower temperatures. The storage stiffness decreased from 3, 540 +/- 40 N/m at 62°C to 1, 200 +/- 90 N/m at 62°C. This indicates that a decrease in crosslinking

density causes a reduction in stiffness and in the glass transition temperature. The same behavior would be expected in macro-scale materials.[10]

Using these DnMA results as a guide, we chose to program the structures with a lower crosslinking density at 67°C. Images from a representative programming sequence are displayed in **Figure S11**, where the orange dashed outline represents the as-printed structure, and the blue one – the programmed configuration. These images display less bending in the pillars during deformation compared with structures printed at higher laser power and programmed at their loss modulus peak temperature (77°C), most probably because the lower programming temperature minimizes lateral stage displacement drift in the instrument. The programmed structures had a characteristic shape recovery ratio of 94 +/- 1%, slightly below that of 96 +/- 3% observed for the high crosslinking density pillars The recovery time (**Video S4**) of 219 seconds exhibited by the lower density samples represents a ~37% increase from the 160 +/- 20 seconds average recovery time for all structures with higher crosslinking density. Both observations are consistent with macro-scale free recovery trends in acrylate networks and illustrate the role of crosslinks in driving shape recovery, i.e. increased shape recovery time and lower shape recovery ratio are caused by decreased crosslinking.[10]

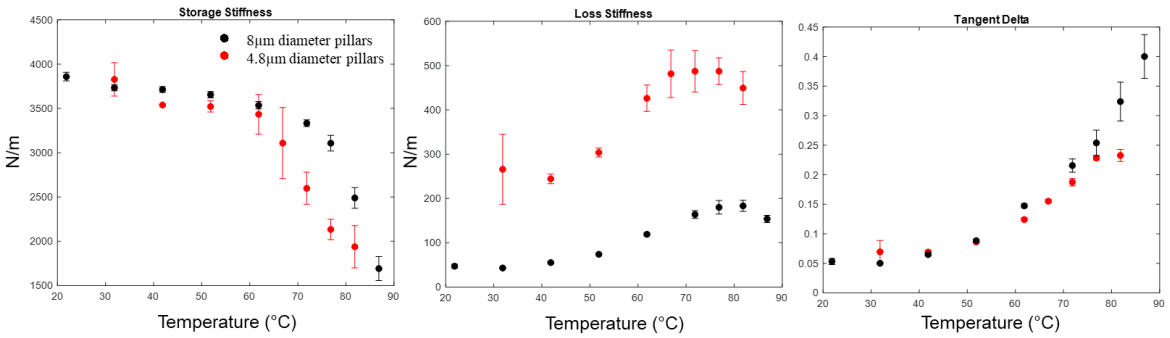

Figure S12. (a) Storage stiffness, (b) loss stiffness, and (c) tangent delta of 8µm diameter pillars (black) and of 4. 8µm diameter pillars (red). N=3 for 4.8µm diameter pillars and n=5 for 8µm diameter pillars.

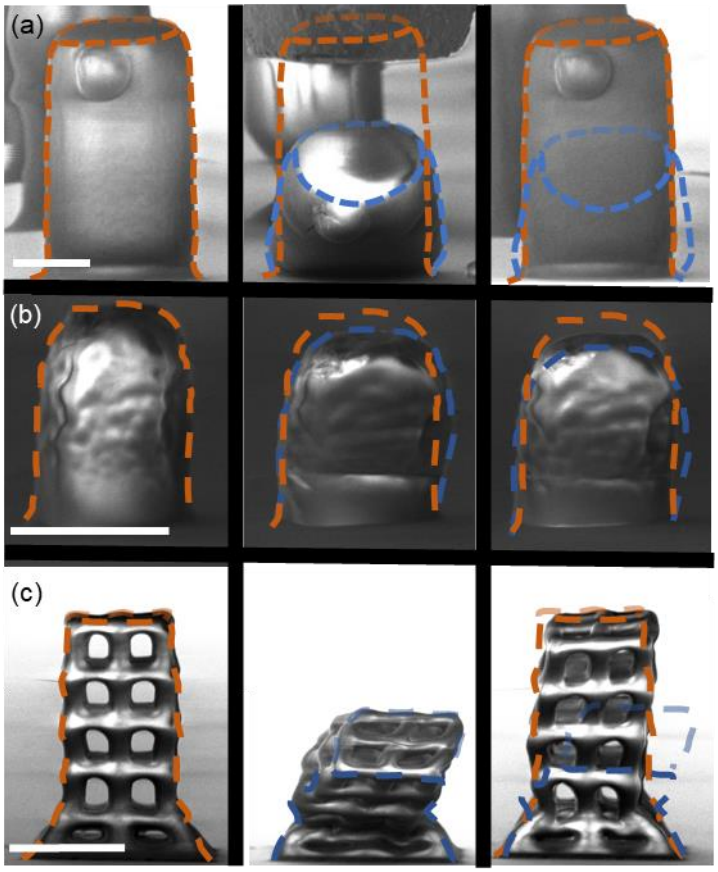

Figure S13. Programming sequence of (a) an 8µm diameter pillar, (b) a 4.8µm-diameter pillar, and (c) a cubic lattice whose solid material volume is equivalent to that of the 4.8um diameter pillar. Image panels correspond to the initial (leftmost), programmed (middle), and recovered (rightmost) states. Outlines of the original structures are provided in orange and outlines of the programmed shapes are provided in blue. Scale bar 5µm in all structures.

Effects of structure size and geometry

We compared the characteristic DnMA and programming properties of pillars with 8µm and 4.8µm diameters. **Figure S12** displays the storage and loss stiffnesses and tangent delta for these samples subjected to 100µN of static load and a 20nm displacement amplitude with the corresponding in-air correction. These results indicate that in the pre-glass transition region tangent delta and storage stiffness are independent of size. The increased loss modulus suggest inscreased energy dissipation and the low tangent delta plateau observed at 82°C suggests a broad glass transition region, which is consistent with expected higher heterogeneity and relative contribution of network defects at decreasing scales.

The morphological manifestation of these results can be observed in **Figure S13**, which displays a characteristic shape memory programming sequences of the samples. A 14% reduction in the shape recovery ratio with size, from the 96 +/- 3%for the 8 μm-diameter pillars to 82% for the 4.8μm dimeter pillar in **Figure S13**, is consistent with the greater degree of heterogeneity within the polymer network observed through the thermomechanical properties (**Figure S12**), because regions of high crosslinking density may not contain flexible chains capable of storing entropic energy. We did not observe significant differences in the recovery speed between samples of different diameters (**Videos S6** and **S2**): 159 seconds for the 4.8μm diameter pillars and 127 seconds for 8μm diameter ones. This indicates that in this experimental setup, the recovery rates may be limited by the heating rate of the sample holder rather than by the volume of the miro-scale sample.

We also explored the effect of structure on shape memory response. We estimated the volume of the 4.8μm cylindrical pillars to be 114 μm^3 and matched it to the material volume of ~119 μm^3 for the cubic lattices, estimated from CAD geometries and SEM images. Any variability in shape recovery between these two types of samples would then be attributed to the geometry, i.e. the >3x greater surface area and a 6x lower minimal feature size in the lattices. The observed shape recovery ratio of 82% for the 4.8μm pillar is within the 86 +/- 4% range observed for cubic lattices, rendering geometric variability inconsequential for shape recovery. This suggests that in this size regime, the variability in the polymer free surface glass transition does not play a major role in shape recovery and that characterization performed on pillars can be used to determine the behavior of more complex structures.[11]

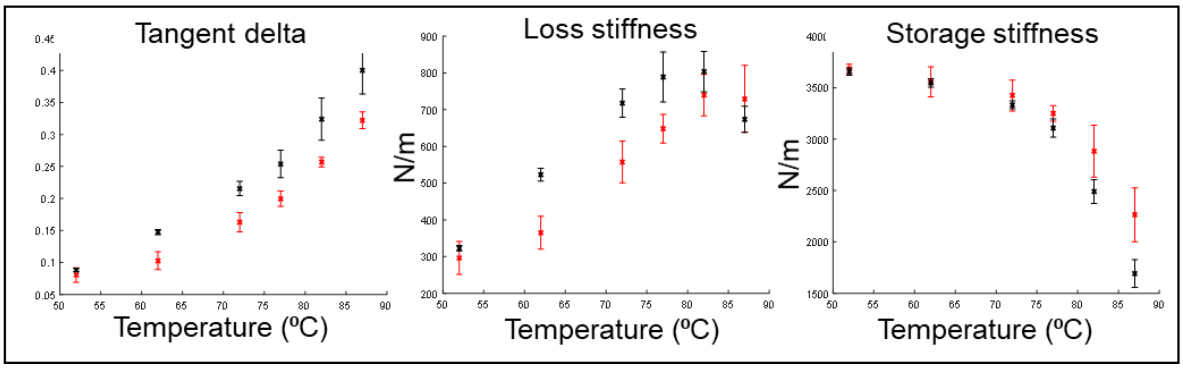

Figure S14. Storage and loss stiffness as well as the tangent delta of the synthesized pillars tested at 10 Hz (black) and 50 Hz (red).

DMA at increased frequency

According to the principle of time-temperature superposition, an increase in the frequency of a DMA experiment should correspond to a decrease in temperature. The DMA characterization was therefore repeated at 50Hz, a frequency for which the one dimensional oscillator was demonstrated to be valid. As compared to the 10Hz experiment, the tangent delta decreased, the peak in the loss stiffness shifted to higher temperatures, and the storage stiffness increased (**Figure S14**). This is consistent with the observed features being a signatures of a glass transition.

References

[1] W. Kuhn, *Naturwissenschaften* **1936**, *24*, 346.

[2] D. L. Safranski, K. Gall, *Polymer* **2008**, *49*,446.

[3] G. Socrates, *Infrared and Raman Characteristic Group Frequencies: Tables and Charts*, John Wiley & Sons, **2004**.

[4] S. E. Barnes, Z. T. Cygan, Z. T., J. K. Yates, K. L. Beers, E. J. Amis, *Analyst* **2006**, *131*, 1027.

[5] E. G. Herbert, W. C. Oliver, G. M. Pharr, *J. Phys. D: Appl. Phys*. **2008**, *41*, 074021.

[6] W. J. Wright, W. D. Nix, *J. Mater. Res.* **2009**, *24*, 863.

[7] S. A. Hayes, A. A. Goruppa, F. R. Jones, *J. Mater. Res*. **2004**, *19*, 3298.

[8] L. J. Jiang, Y. S. Zhou, W. Xiong, Y. Gao, X. Huang, L. Jiang, T. Baldracchini, J. F. Silvani, Y. F. Lu, *Opt. Lett.* **2014**, *39*, 3034.

[9] I. S. Ladner, M. A. Cullinan , S. K. Saha, *RSC Advances*, **2019**, *9*, 28808.

[10] C. M. Yakacki, R. Shandas, C. Lanning, B. Rech, A. Eckstein, K. Gall, *Biomaterials* **2009**, *28*, 2255.

[11] B. Li, X. Lu, Y. Ma, X. Han, Z. Chen, *ACS Macro Lett*. **2015**, *4*, 548.